Received 8 October 2023; revised 9 November 2023; accepted 20 November 2023. Date of publication 27 November 2023; date of current version 30 January 2024.

Digital Object Identifier 10.1109/OJAP.2023.3336762

Wideband and Wide Beam Scanning Dual-Polarized Phased Array Antenna-in-Package Design for 5G Applications

HAORAN ZHANG (Student Member, IEEE), AND ATIF SHAMIM (Senior Member, IEEE)

Computer, Electrical, and Mathematical Sciences and Engineering Division, King Abdullah University of Science and Technology, Thuwal 23955, Saudi Arabia

CORRESPONDING AUTHOR: H. ZHANG (e-mail: haoran.zhang@kaust.edu.sa)

This work was supported by the CEMSE Division at King Abdullah University of Science and Technology, Saudi Arabia, under Grant BAS/1622/01-01.

ABSTRACT Millimeter (mmWave) 5G phased arrays require multiple simultaneous features for reliable high data-rate communication. However, it is challenging to simultaneously achieve a true wideband operation for all parameters due to mutual coupling and grating lobe issues. A 5 × 5-stacked patch rectangular phased array was designed and fabricated in a 15-layer low-temperature co-firing ceramic (LTCC) substrate. This work utilized multiple design strategies, such as employing stacked patch topology, electromagnetic band gap (EBG) structures, and the rotation of elements to obtain a true wideband performance. The single element of the phased array was a dual linear polarized stacked patch antenna with notched corners. Compared to a standard patch antenna, the bandwidth was enhanced by 15.3%. The undesired mutual coupling between elements was minimized by rotating nearby elements and introducing EBG structures between the adjacent elements. A wideband beamforming network composed of a Rotman lens and a 5-way Wilkinson power divider (WPD) was also designed and fabricated. The proposed phased array achieved 6 GHz of bandwidth, covering 24 to 30 GHz and achieving a maximum gain of 17.5 dBi and a wide beam-scanning range from –50 to +50 degrees. This work also introduced a figure of merit (FoM) based on all critical performance parameters for objective comparison with state-of-the-art designs. The proposed design achieved the highest FoM (0.451), whereas most similar 5G phased array designs achieved much lower FoM value.

INDEX TERMS Phased array, low-temperature co-firing ceramic, beam scanning, millimeter 5G.

I. INTRODUCTION

As WIRELESS mobile technology evolves at an accelerated pace, there's an increasing need for faster data transmission speeds, particularly in mmWave 5G bands essential for applications, such as enhanced mobile broadband (eMBB), massive machine-type communications (mMTC), and ultra-reliable and low latency communications (uRLLC) [1], [2]. Notably, mmWave 5G bands present larger available bandwidths compared to the commercialized sub-6 GHz 5G and 4G bands. Therefore, they can support a much higher data-rate communication system, according to Shannon theory [3]. mmWave Phased array antennas are an integral part of 5G systems, and their wideband operation is critical for achieving the required goals of high data rates. Phased arrays that cover multiple mmWave 5G frequency bands (such as the three bands in the range of 24–30 GHz [4]) can also reduce the system deployment cost. However, it is challenging to optimize all performance parameters, such as large beam scanning angles, low side-lobe levels, low mutual coupling, and high realized gain simultaneously for the entire bandwidth [5]. However, a high-gain antenna array is necessary because of the significant atmospheric attenuation and penetration loss of the EM waves at the mmWave 5G frequency range [6].

As illustrated in Fig. 1, it is also critical to realize wide beam scanning capability to ensure enhanced communication coverage while reducing the deployment cost of 5G antenna systems. Moreover, communication capacity and spectrum efficiency can be boosted by utilizing a dual-polarization antenna system. Grating lobes, another major issue in array

© 2023 The Authors. This work is licensed under a Creative Commons Attribution-NonCommercial-NoDerivatives 4.0 License.
For more information, see https://creativecommons.org/licenses/by-nc-nd/4.0/

TABLE 1. Comparisons of different state-of-the-art mmWave 5G phased array designs.

Ref *	Antenna Technology	Bandwidth (GHz)	Number of elements	Realized Gain (dBi)	Beam scanning range	Dimensions (mm^3)	Polarization	Gaps
[7]	Sequential rotation fed dual-polarized patch	29.5–30	32 × 32	~ 32.9	H: ±60° V: ±60°	160 × 160 × 1.9	Dual	**Narrow BW**
[8]	Probe-fed patch antenna	28.5–30.5	4 × 8	~ 19	H: ±50° V: ±25°	25.2 × 40 × 0.91	Single	**Narrow BW**
[9]	Parasitically gap-coupled patch	26–29	8 × 8	21.5	H: ±45° V: ±45°	46 × 52.7 × 1.65	Single	**Narrow BW**
[10]	PCB-integrated stacked patch antenna	28–32	8 × 8	22.5	H: ±25° V: ±50°	50 × 63 × 1.32	Single	**Bad Coverage**
[11]	Tightly coupled dipole array	23.5–29.5	8 × 8	~ 16	H: ±60° V: ±60°	85.6 × 85.6 ×3.7	Dual	**Low Gain**
[12, 13]	Slotted waveguide array	26.5–31	8 × 8	24	H: ±45° V: ±10°	72 × 72 × 1.32	Dual	**Bad Coverage**
[14]	Air cavity backed patch antenna on lid substrate	28–32	8 × 8	24	H: ±50° V: ±50°	70 × 70 × 2.7	Dual	**Narrow BW**
[15]	Cavity-backed patch antenna	27.8–29.5	2 × 4	13	H: ±50° V: ±40°	11.6 × 22 × 0.756	Dual	**Narrow BW**
[16]	Dielectric resonator antenna arrays	26–30	8 × 8	23.5	H: ±60° V: ±60°	63.1 × 69.4 × 3.6	Dual	**Large Size**
[17]	Surface-mounted Vivaldi array	26–40	8 × 8	19 - 22	H: ±50° V: ±50°	31.5 × 31.5 × 10.9	Dual	**Large Size**
[18]	Coaxial-fed stacked patch antenna	23.5–29.5	8 × 8	21.7 – 23.7	H: ±40° V: ±40°	46 × 43 × 1.5	Single	**Bad Coverage**
[19]	Single-polarized surface-mounted Vivaldi array	10–35	8 × 8	23.4	H: ±45° V: ±45°	36 × 36 × 22.5	Single	**Large Size**
[20]	Coaxial-fed stacked patch antenna	27–31	32 × 32	33.6	H: ±60° V: ±60°	149.5 × 149.5 × 1.5	Dual	**Narrow BW**
[21]	Stamped metal antenna in package, serving as heat sink simultaneously	28.15-28.85	1 × 8	13.78	H: -46°/+44°	80 × 40 × 1.2	Single	**Narrow BW**
[22]	Stacked patch antenna array with metal vias wall separation	22.6–27.35	8 × 8	16.0	H: ±45° V: ±45°	72 × 72 × 3.6	Single	**Large Size**
This work	Stacked patch with notched corners, EBG, and element rotation	24-30	5 × 5	17.5	H: ±50° V: ±50°	42.5 × 42.5 × 1.5	Dual	

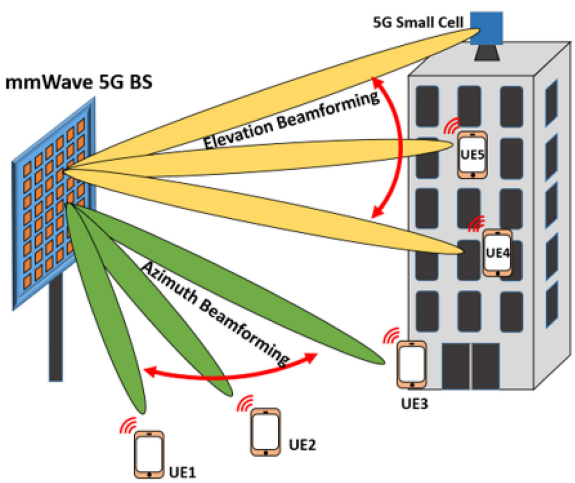

FIGURE 1. An illustration of an mmWave 5G phased array base station with beam scanning capability in the elevation and azimuth plane.

antennas, can be avoided by designing a dense array. However, the dense array could lead to high mutual coupling between the adjacent elements, which, in turn, would deteriorate the array gain and wide beam scanning capability. Therefore, it is imperative to suppress the mutual coupling level between the array elements. Though all the performance parameters can be achieved individually, maintaining a large bandwidth for all of them simultaneously can be challenging because of their interdependencies and tradeoffs, making the design a multi-dimensional optimization problem.

Considerable research efforts have been made to tackle these design challenges of mmWave 5G phased arrays [7], [8], [9], [10], [11], [12], [13], [14], [15], [16], [17], [18], [19], [20], [21], summarized and compared in Table 1. However, most works have focused on only one or two performance parameters. For example, in [19], a surface-mounted Vivaldi array was shown, obtaining a large bandwidth of 25 GHz (10–35 GHz). Nevertheless, it was a single-polarized antenna with bad array compactness because the Vivaldi antenna's traveling wave required large dimensions. In another example, a dual-polarized slotted waveguide array was shown in [12], [13], achieving a high gain of 24 dB with only 64 elements, and the design was relatively compact. However, the beam scanning performance was not great and only achieved +/– 10 degrees in one of the orthogonal planes. In another example [20], a coaxial-fed

stacked patch array achieved dual-polarization, a good beam scanning angle (up to +/– 60 degrees), a high realized gain, and good compactness. However, though a relatively large bandwidth of 4 GHz (13.8%) was realized, it was still not large enough to cover all the three mmWave bands between 24–30 GHz. For reference, the limitations of these published works are highlighted in Table 1. Indeed, until now, no published work has demonstrated the optimization of all performance parameters for the entire 5G bandwidth (24–30 GHz).

This work introduces different design techniques to optimize the phased array from all aspects simultaneously for the entire bandwidth. Thus, a 5 × 5 rectangular phased array was designed and fabricated in a multilayered LTCC substrate due to its low-loss mmWave performance, good packaging properties, and high-level integration. For wideband performance, a dual linear polarized stacked patch antenna with notched corners was designed as the element for the phased array. Moreover, the orientations of individual elements were optimized, and EBG structures were incorporated between them to minimize the mutual couplings between the neighboring elements in the array while achieving a wide beam-scanning range. Finally, a wideband beamforming network was designed to verify the proposed array's performance. Measurements showed that the phased array achieved a maximum gain of 17.5 dBi and a beam scanning range of –50 to +50 degrees over the desired 6 GHz bandwidth (24–30 GHz), covering the three most promising mmWave 5G frequency bands in K–/Ka bands (n257, n258, n261) [4]. Furthermore, an FoM derived for the objective comparison of mmWave 5G phased arrays confirmed the simultaneous optimization of all critical parameters, ensuring one of the highest FoM values for the design presented in this paper.

The structure of this article is outlined belows. Section II presents the design of the antenna element. Section III shows the detailed design for the phased array in simulations along with its feeding network. A design of a wideband beamforming network composed of a Rotman lens and five five-way WPDs is demonstrated in Section IV. Finally, Section V presents the measured results and the analysis for the antenna element and the entire phased array.

II. ANTENNA ELEMENT DESIGN

This section first introduces the LTCC technology and discusses its suitability for the phased array design. Then, the design of the single element is presented, particularly from the perspective of bandwidth enhancement.

A. LTCC TECHNOLOGY AND THE ANTENNA STACK-UP

Ferro A6M LTCC technology was chosen in this work because it offers reliable multilayered implementation, low dielectric loss in the mmWave range, and excellent thermal and packaging properties [21]. Fig. 2 depicts the stack-up of the Ferro A6M LTCC substrate, showing the 16 layers utilized in this work. The thickness of each layer

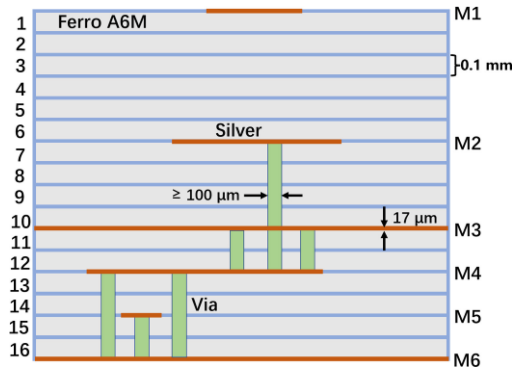

FIGURE 2. Stack-up of the 16-layer Ferro A6M LTCC substrate.

was 0.1 mm. The dielectric constant for this material was 5.76, slightly high for antenna implementation. However, it offered a low loss tangent of 0.001 at 30 GHz and a high conductivity silver as the metallization option [22]. The low loss and the ability to develop multilayered structures made this process quite suitable for efficient and compact 5G antenna designs. Moreover, the LTCC material had high thermal conductivity (2 W/mK), low thermal expansion (7 ppm/K), and decent hermetic sealing capability (low water absorption) [22]. As a packaging material, these protective features are crucial to safeguard driving circuits and antennas under high power scenarios or challenging conditions

B. SINGLE-ELEMENT DESIGN WITH A FOCUS ON LARGE BANDWIDTH

As a starting point, the microstrip patch antenna was selected and designed as depicted in Fig. 3(a) due to its features of low profile, less complexity, and high element gain. However, it is well known that the conventional microstrip patch antenna is narrow-band because it is a single resonance-based antenna. The black curve in Fig. 4 shows the reflection coefficient of a conventional patch antenna as depicted, which has a bandwidth of only 2.4 GHz (8.8%). Since a wide operating bandwidth was desired (24–30 GHz, 22.2%), achieving a wide impedance bandwidth for the single element was critical.

To achieve a wider impedance bandwidth, a second resonant structure can be combined with the patch antenna. Therefore, in this work, a parasitic patch was stacked on top of the original driven patch with a separation of 0.6 mm to create the second resonance slightly away from the first resonance. In this structure, as shown in Fig. 3(b), the main (driven) patch was responsible for the low-frequency resonance, while the stacked (parasitic) patch played a major role in the high-frequency resonance. By adjusting the dimensions of the driven and stacked patches, the dual resonance frequencies were aligned to create a broader frequency range, leading to an improved bandwidth. With the help of the stacked patch, the impedance bandwidth was increased to 4.7 GHz (17.4%), as illustrated by the green curve in Fig. 4. Notably, the high-frequency resonance

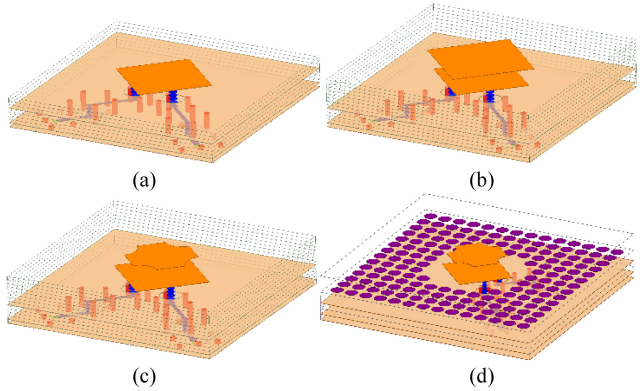

FIGURE 3. Bandwidth enhancement: antenna element designs (a). probe-fed single patch, (b). stacked patch antenna, (c). stacked patch with notched corners, (d). corner notched stacked patch with EBG.

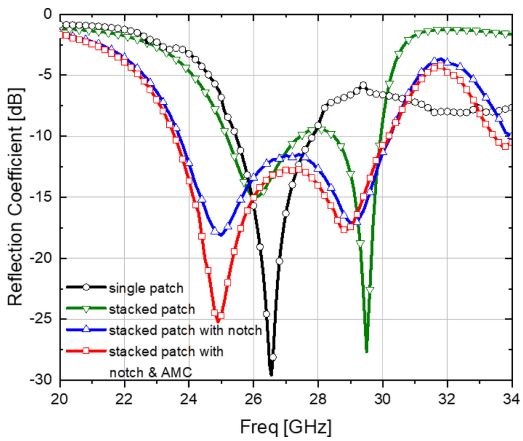

FIGURE 4. Impedance bandwidth improvement.

had a remarkably high-quality factor compared to the low-frequency resonance. This bandwidth, though enhanced, was still lower than the required bandwidth. Thus, four notches were introduced in the stacked patch corners to further improve the bandwidth, as shown in Fig. 3(c). These notches progressively changed the length of the stacked patch along the current direction for both polarizations, which is the main reason for bandwidth enhancement. As shown in Fig. 4, a wide impedance bandwidth of 6.5 GHz (24.1%), covering from 23.7 GHz to 30.2 GHz, was achieved (blue curve).

C. FINAL ANTENNA ELEMENT DESIGN

Figure 5 illustrates the final design of an antenna element on an LTCC substrate. A stacked patch with notched corners is positioned above the probe-driven patch antenna. there are period unit on the same horizontal level as that of the driven patch. The periodic structures were designed for mutual coupling reduction and will be discussed in detail in Section III. The influence of the periodic structures on the antenna element's impedance bandwidth was evaluated, as discussed later in this section.

As shown in Fig. 5(a), this multilayered structure had three ground layers. The GND 1 layer served as both the antenna's ground plane and also confined the horizontal

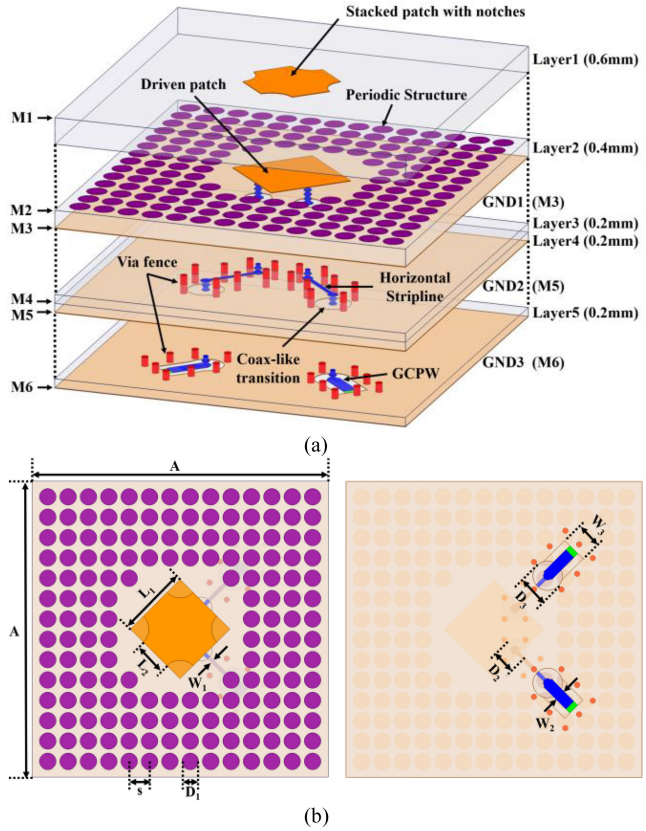

FIGURE 5. The geometry of the single antenna element: (a) exploded view, (b) top view, and (c) bottom view.

transition zone in conjunction with the GND 2 layer. The GND 3 layer was implemented to isolate the RF signal transmission from the signal routing of the beamforming network. The RF signal was transmitted to the driven patch between GND 1 and GND 3 using an integrated system that included a grounded coplanar waveguide (GCPW), a coaxial-like vertical transmission channel, a stripline, and a vertical probe, as depicted in Fig. 5. The vertical transmission line, resembling a coaxial design, features a central signal via, accompanied by four peripheral vias. These surrounding vias play a key role in guiding the EM waves and fine-tuning the characteristic impedance by modifying the overall diameter. While, the stripline locates at Layer 3 and is shielded with top (Layer 2) and bottom (Layer 4) grounds. The coax-like line and stripline were designed for vertical and horizontal RF signal transmission, respectively. These topologies were selected due to their low radiation loss at the mmWave bands. In addition, to reduce crosstalk between neighboring transmission lines, two parallel rows of vias were introduced to the stripline, spaced at a guided quarter-wavelength interval. It was essential to reduce this crosstalk because it is considered to be one of the primary factors contributing to mutual coupling and parallel plate mode through the substrate in a phased array design. Table 2 lists all geometric parameters of the antenna, shown in Fig. 5.

Fig. 6 illustrates the geometry and simulation results of the antenna element's feeding line, combining a GCPW, a

TABLE 2. Dimensions of the proposed antenna element in Fig. 5 (Unit: mm).

A	W_1	W_2	W_3	D_1	D_2	D_3	L_1	L_2	s
7	0.1	0.3	0.7	0.45	0.6	0.8	1.9	1.1	0.55

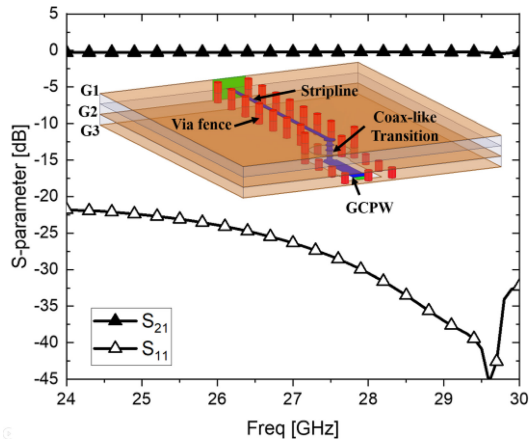

FIGURE 6. The geometry of the antenna feeding line and its simulation results.

coax-like vertical transition, and a stripline. The total length of the feeding line was 2.7 mm with an insertion loss of only 0.1 dB, which was quite small for this frequency range. Furthermore, the S_{11} parameter was well-matched (below –20 dB) over the entire desired frequency range.

Fig. 7 (a) and (b) show the simulated results of the antenna element. The proposed antenna configuration offers a wide impedance bandwidth spanning 6.5 GHz, ranging from 23.7 GHz to 30.2 GHz. Furthermore, it maintained a low crosstalk level (< –16 dB) between the horizontal and vertical polarizations, as demonstrated by S_{21} (red curve in Fig. 7(a)). This low crosstalk level between the two polarizations was critical for decent channel isolation in the communication system. In addition, the 3-dB gain bandwidth spanned an extensive frequency spectrum from 21.5 GHz to 31.2 GHz. Notably, between 24 GHz and 30 GHz, the gain fluctuation was limited to 0.6 dB. Fig. 7(b) demonstrates the polarization purity by comparing co-pol and cross-pol radiation patterns. It shows that the difference between the co-pol and the cross-pol was always larger than 17 dB over the desired frequency range. As depicted in Fig. 7(b), the half-power beamwidth always covered the angle from –50 to +50 degrees for the entire frequency range. The wide beam feature of the antenna element was crucial for the implementation of the phased array with wide beam scanning capability.

III. PHASED ARRAY CONFIGURATION

The next step in the design was to utilize the proposed antenna element to construct the complete phased array. However, there were two major issues associated with the phased array design. One was the grating lobe issue, while the other was the mutual coupling issue. This section proposed different design techniques to tackle these two

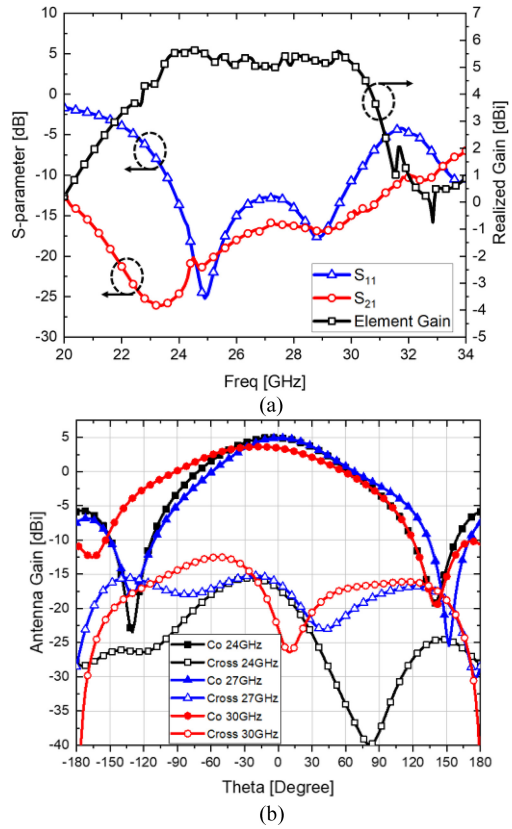

FIGURE 7. Simulation results of the antenna element: (a) S-parameter and realized gain versus frequency, (b) co-pol versus cross-pol.

major issues. The final phased array design is also shown in this section.

A. GRATING LOBE FREE DESIGN

The element spacing was one of the most critical factors affecting the grating lobe. Due to the large operational bandwidth, the same element spacing corresponded to different electrical lengths at different frequencies. For example, assuming that the element spacing was equal to 6.8 mm, the element spacing would correspond to 0.544λ at 24 GHz, but at the same time, it was equivalent to 0.68λ for the high-frequency band (30 GHz). Therefore, when the main beam was scanned at +50 degrees at 30 GHz and 27 GHz, there would be a grating lobe around –50 degrees. This can degrade the overall array performance. Hence, the element spacing needed to be optimized to avoid grating lobes in the desired beam scanning area.

It is well known that the phase shift between two elements should be equal to the following formula for a rectangular array [23]:

$$\Delta\Phi = \frac{2\pi d}{\lambda} sin(\theta) \tag{1}$$

$$\theta = arcsin\left(\frac{\Delta\Phi + m \times 2\pi}{2\pi} \times \frac{\lambda}{d}\right), m = 0, \pm1, \pm2, \ldots \tag{2}$$

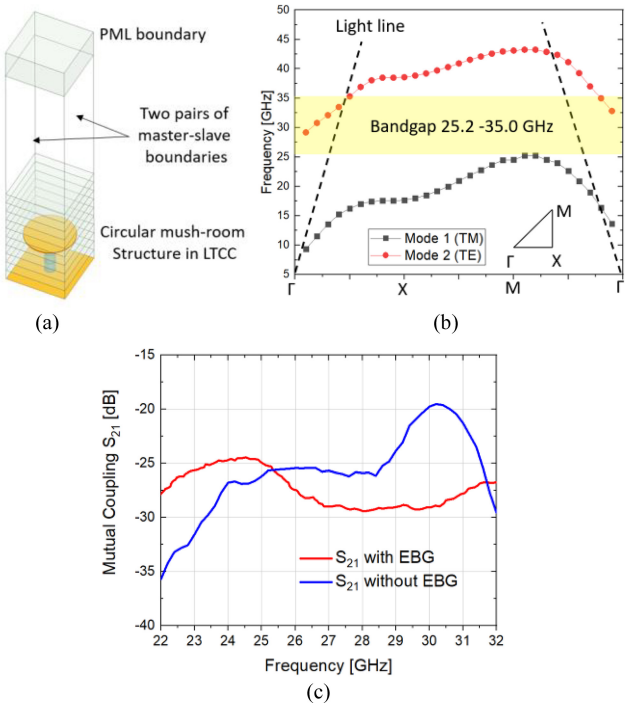

FIGURE 8. (a) HFSS simulation model of the EBG unit cell, (b) dispersion diagram of the simulated EBG structure, (c) mutual coupling level comparison between the cases with and without EBG structure.

where θ is the beam scanning angle, and d is the element spacing. Then the maximum spacing D_{MAX} for grating lobe free within $[-\theta_{MAX}, +\theta_{MAX}]$ can be derived as follows:

$$d_{MAX} = \frac{\lambda}{1 + |sin(\theta_{MAX})|}, \theta_{MAX} \in \left[\frac{-\pi}{2}, \frac{+\pi}{2}\right] \quad (3)$$

The maximum spacing for the desired beam scanning range of –50 to +50 degrees can be found in equation (3). Based on this calculation, the grating lobe could be avoided for the desired beam scanning range over the entire bandwidth as long as the D_{MAX} was smaller than 5.66 mm. Moreover, the element spacing needed to be reduced to achieve a larger beam scanning range without the grating lobes. Nevertheless, this reduction could cause a much higher mutual coupling between the adjacent elements. Therefore, the element spacing of 5.5 mm ensured that while scanning the main beam up to +50 degrees, the array factor at –50 degrees was always more than 10 dB lower than the main beam for the entire frequency range of 24–30 GHz.

B. EBG STRUCTURE

To minimize the mutual coupling between the neighboring antennas, a circular mushroom-like EBG is introduced in the antenna array. The specially designed EBG structures can create a high-impedance surface that blocks the surface wave propagation between adjacent elements for specific frequency bands. Fig. 8(a) illustrates the high-frequency structure simulator (HFSS) simulation model of the EBG unit cell, where the perfect matched layer (PML) boundary was placed on the top, and the two pairs of master-slave boundaries were applied to the side surfaces of the unit cell to realize the periodicity.

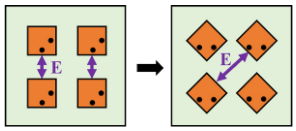

FIGURE 9. Array element self-rotation.

The Bloch-Floquet theorem, used to characterize the performance of EBG structures, can indicate the wave propagation properties in an infinite media that comprises periodic elements [24]. According to the theory, a unit cell with periodic boundary conditions can fully calculate the wave propagation characteristics in a periodic structure [25]. Furthermore, the wave propagation vectors of a unit cell can be defined in the Brillouin zone [26]. The complete properties of the periodic structure can be acquired once all the propagation vectors are determined in the Brillouin zone. Therefore, the dispersion diagram starts from Γ (0 degrees, 0 degrees) to X (0 degrees, 180 degrees), then to (180 degrees, 180 degrees) and back to Γ, for a two-dimensional periodic EBG structure, as demonstrated in Fig. 8(b).

The dispersion relation of this EBG unit was calculated with the eigenmode solver in HFSS, plotted in Fig. 8(b). It shows both the TM and TE mode propagation performance. The band gap for this periodic structure was from 25.2 to 35.0 GHz. Within this frequency range, the surface waves were suppressed, thus reducing the mutual coupling. However, it should be noted that this was in the ideal case where the EBG structure was infinitely large. To verify the functionality of the EBG structure, the simulation for the cases with and without EBG is conducted and the simulation comparison is plotted in Fig. 8(c). It shows that the case with the EBG structure presents a lower mutual coupling level, especially in the frequency range of 26–31 GHz, which also corresponds to the bandgap of the EBG structures implemented.

C. 45-DEGREE ELEMENT ROTATION

To further reduce the mutual coupling, an element rotation technique was applied. In the conventional design, the adjacent antennas' mutual coupling mainly happens along the E-plane, which is the radiation aperture. This is because the two adjacent antennas radiating apertures are close to each other. However, by applying a 45-degree rotation to each element, the distance between the two adjacent radiation apertures became much larger, as shown in Fig. 9. Consequently, it reduced the mutual coupling between the adjacent elements. This effect was verified by the simulation results depicted in Fig. 10.

As seen in Fig. 10, a good beam scanning range was achieved in the H-plane from –50 to + 50 degrees before the 45-degree rotation. However, there was a significant drop in the E-plane when the scanning angle was larger than 30 degrees, which is mainly caused by the strong mutual

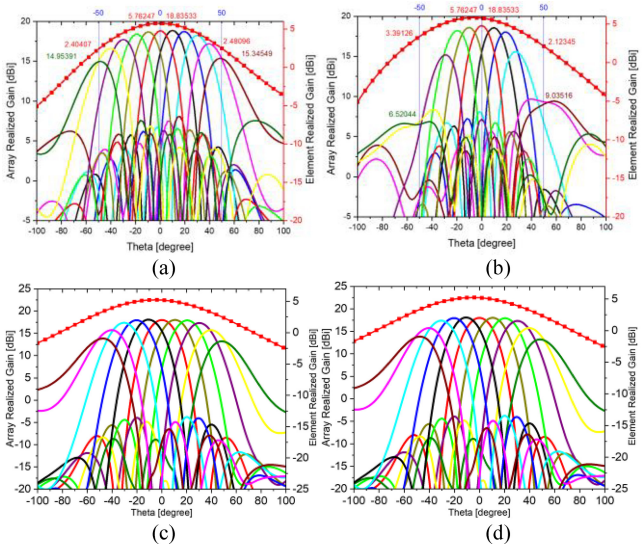

FIGURE 10. Simulation results of the phased array's beam scanning capability. Before the 45-degree element rotation, (a) H-plane, (b) E-plane. |After the element rotation, (c) H-plane and (d) E-plane.

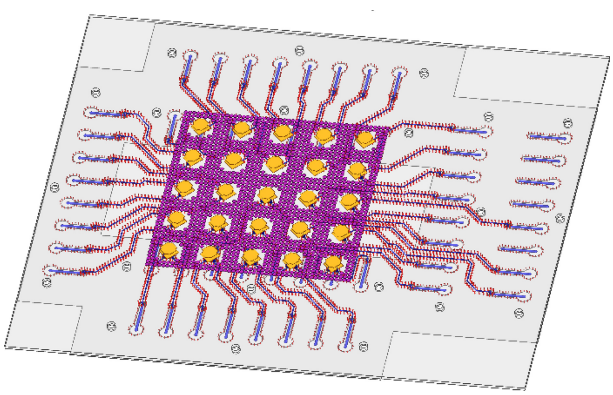

FIGURE 11. HFSS simulation model of the complete phased array alongside its associated feed network.

coupling between the adjacent elements along the E-plane. After the 45-degree rotation, beam scanning was achieved in both the E-plane and H-plane from –50 to +50 degrees. Therefore, it can be concluded that the 45-degree element rotation successfully suppressed the mutual coupling.

Fig. 11 demonstrates the HFSS simulation model of the complete phased array alongside its associated feed network. In the HFSS simulation, the component array domain decomposition method (CADDM) was utilized to simulate this 5 x 5 stacked patch antenna with its feeding network for better simulation efficiency. Compared to a single-element structure, shown in Fig. 5(a), the feeding line of each element in the array was extended and curved for routing. Eventually, the array simulation shows a maximum realized gain of 18.3 dBi and a decent radiation efficiency of 88.7%.

IV. BEAMFORMING NETWORK DESIGN

Furthermore, a wideband beamforming network, incorporating a Rotman lens coupled with five 5-way WPDs, has been developed and tested to validate the wide bandwidth and wide beam steering potential of the proposed antenna array. The reasons for selecting this beamforming scheme were that it could realize multiple beams on demand and both the Rotman lens and the multi-stage WPD are wideband structures. An alternate choice could have been the conventional butler matrix. However, it offered a limited number of beams and required multiple phase shifters, restricting the overall bandwidth of the beamforming network. In this work, the Rotman lens formed the desired linear phase differences between the array ports for beam steering. Then, five 5-way WPDs were applied to each array port to equally split the RF power and feed 25 antenna array elements through the onboard RF connector jacks. The beamforming network was designed and fabricated in a four-layer Rogers 4350B printed circuit board (PCB).

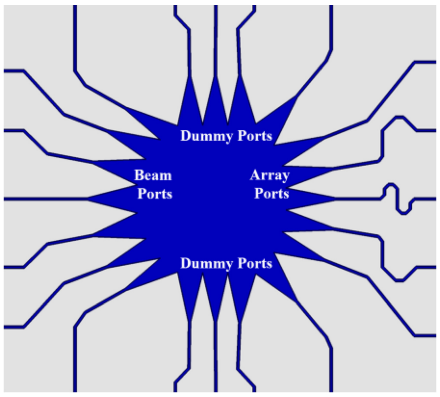

FIGURE 12. HFSS simulation model of the Rotman lens beamformer.

A. WIDEBAND ROTMAN LENS DESIGN

There are different types of phased array beamforming networks, such as the Butler matrix, the Rotman lens, and the active beamforming integrated circuit (IC) [27], [28], [29], [30], [31]. As mentioned above, the Rotman lens has been widely used among all types of beamforming networks due to its wideband features and less complexity since no circuit components are needed [32], [33], [34]. Fig. 12 illustrates the HFSS simulation model of the designed Rotman lens beamformer. It was made of a microstrip cavity with an input contour and an output contour on the two sides. The input ports, known as beam ports, were evenly distributed on the input contour. Each input port corresponded to an array beam. While, the output contour contained the desired number of output ports, known as array ports, connected to all phased array ports via transmission lines. When one beam port is activated by the RF signal, the signal would be transmitted to all array ports through the Rotman lens with linear phase shifts between each other due to the designed differences in the length of electrical connections among the array ports. The true-time delay performance of the Rotman lens qualified it as the best candidate for applications demanding a wide beam-scanning range over a wide bandwidth.

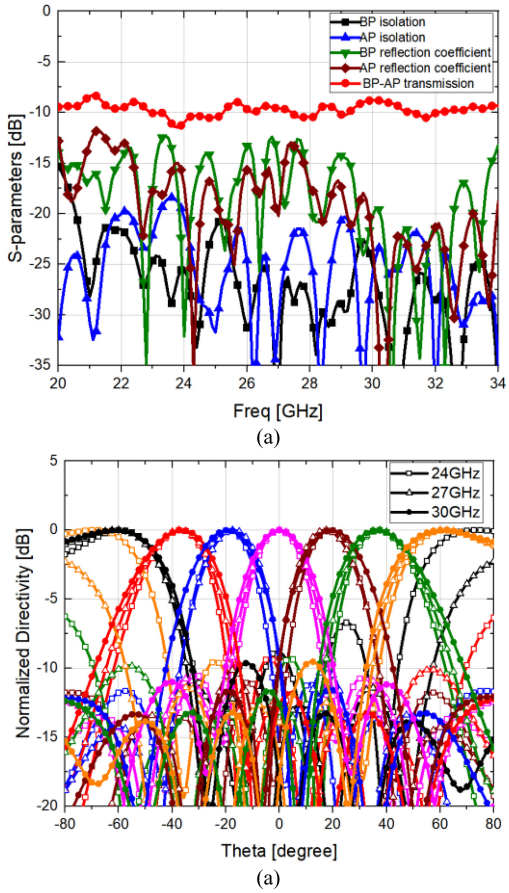

FIGURE 13. Rotman lens beamformer simulation results: (a) reflection coefficients of beam port and array port, (b) normalized beam scanning patterns.

This proposed lens design had seven beam ports (input), five array ports (output), and eight dummy ports. Fig. 13(a) demonstrates the simulated S-parameters of the proposed Rotman lens. The coupling between the beam ports and array ports for this lens at operation frequency (24–30 GHz) was below –20 dB. Moreover, the reflection coefficients of the beam and array ports showed that the S-parameters were less than –10 dB, indicating good impedance matching. In addition, the transmission loss from the beam port to the array was in the range of –9 to –11 dB in the frequency range of 24–30 GHz. To verify that the path delay of the Rotman lens is independent of frequency, the beam-scanning angles at 24 GHz, 27 GHz, and 30 GHz were simulated by feeding different Rotman lens input ports and computing the corresponding array factor based on its output. Fig. 13(b) depicts the normalized beam scanning patterns of the lens at different frequencies. It shows that the beam scanning angle remained approximately constant with frequency. In addition, as expected, the seven beams were steered at around ±57, ±38, ±19, and 0 degrees.

B. FIVE-WAY WILKINSON POWER DIVIDER DESIGN

The proposed phased array had 5 × 5 elements, while the Rotman lens only had five output ports to feed five rows or columns of the array. Therefore, designing a wideband 5-way power divider was necessary to split each output of the Rotman lens into five equal signals and feed all the array elements on a row or a column. This section demonstrated a wideband 5-way WPD design that works in the frequency band of 17.8 to 32.5 GHz by utilizing multi-section and arbitrary power division concepts [35], [36]. It was challenging to realize an odd-number power divider since an equi-amplitude and equi-phase power division was required across all output ports over a wide frequency range. In the proposed design, the Wilkinson power divider is split into multiple sections and each section involves arbitrary power division. The power division ratio of each section was synergistically designed so that the same phase and amplitude were realized across the five output ports.

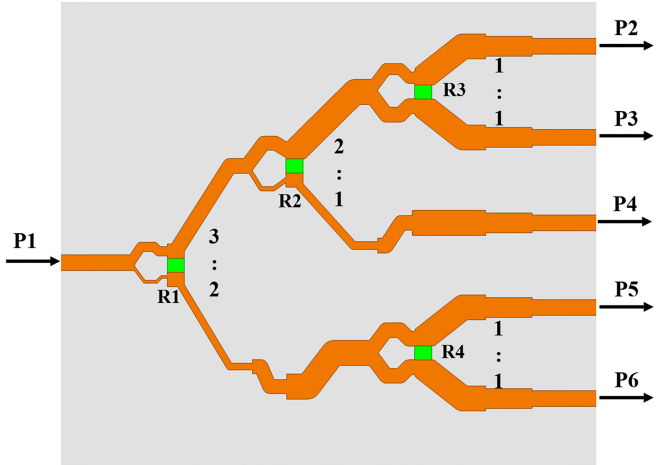

FIGURE 14. Layout of the 5-way Wilkinson power divider.

Fig. 14 demonstrates the proposed 5-way WPD consisting of two equal power division sections and two unequal power division sections. The arbitrary power division was implemented by adjusting the characteristic impedance of each branch's transmission line and the isolation resistor [37]. It shows that a WPD with a 3:2 power division ratio was applied to the input stage. The top branch was further split by a 2:1 WPD and a 1:1 WPD, while the bottom branch was followed by a 1:1 WPD. Then, the equi-amplitude power division was obtained by this proposed multi-section design. To implement equi-phase output over all output ports, the electrical length of each branch was designed to be the same.

Fig. 15 depicts the reflection coefficients of the input port and all output ports which are all well below –10 dB in the frequency range of 17.8 to 34.5 GHz, indicating good impedance matching. Moreover, the insertion loss of the transmission from the input to each output port was around –7.8 dB to –8.8 dB in the desired frequency range. This is a low insertion loss design, considering there was a -7 dB intrinsic insertion loss of a 5-way power divider in an ideal case. In addition, the amplitude variation between all output ports at one frequency was relatively small, between

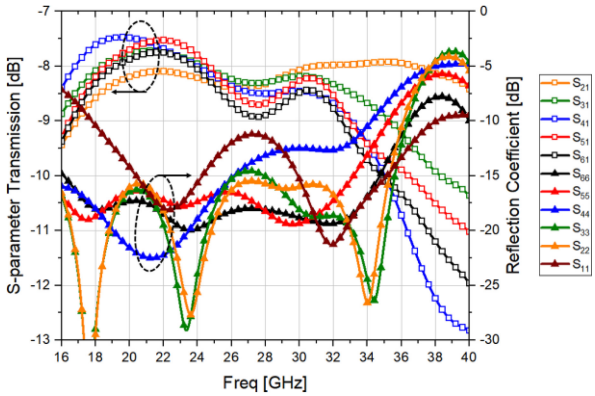

FIGURE 15. Simulated S-parameters: transmissions and reflection coefficients.

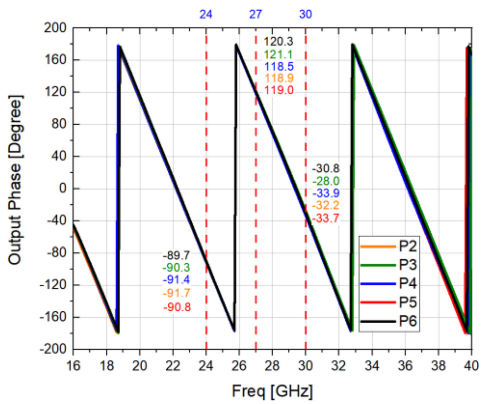

FIGURE 16. The 5-way WPD's output phases vs. frequency.

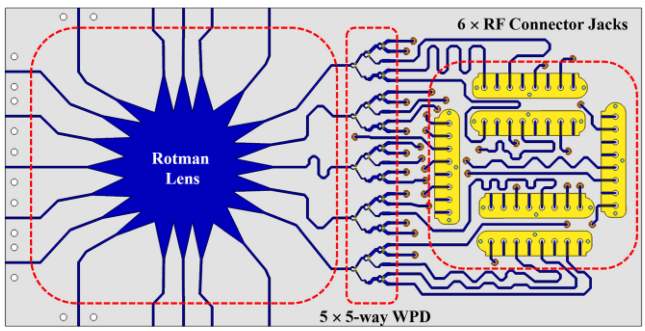

FIGURE 17. Layout of the overall beamforming network.

0.4 dB to 0.6 dB, implying that an equi-amplitude power division was achieved. Fig. 16 shows the phases of all output ports versus frequency. The phase variation between each output port was within an average of ±1.5 degrees, which is considered as a decent equi-phase power division.

Once the designs of the Rotman lens and five-way WPD were ready, the overall beamforming network was designed, as shown in Fig. 17. The Rotman lens first formed the linear phase differences between the array ports by exciting different beam ports. Then, five 5-way WPDs were applied to each array port to equally split the RF power and feed 25 antenna array elements through six RF connector jacks. Microstrip lines are used to connect between the WPDs and the RF connector jacks. Because of the limited space for

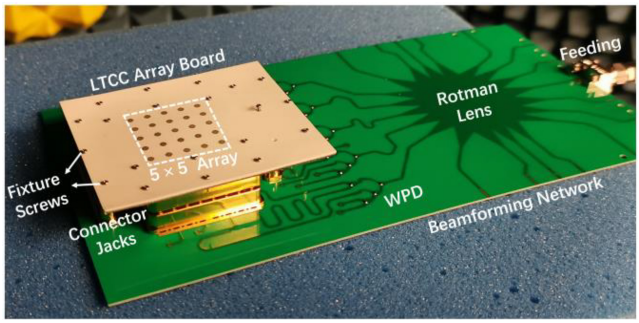

FIGURE 18. Fabricated phased array antenna in LTCC board (white) and beamforming network in PCB (green).

connecting 25 elements, the microstrip lines are utilized on two sides of the PCB to achieve line crossing. Moreover, the length of the microstrip lines is specially designed to make sure equal phase variation on each path.

V. ANTENNA FABRICATION AND CHARACTERIZATION

To validate the design concepts, the Ferro A6M LTCC fabrication process was selected for the implementation of the complete phased array alongside its associated feed network because of its good features of reliable multilayered implementation, low dielectric loss in the mmWave range, and its excellent thermal and packaging properties [21]. The dimensions of the complete LTCC array board were 73.4 mm × 62.8 mm × 1.6 mm, with 16 layers in total. Meanwhile, the beamforming network was fabricated using a low-cost four-layer PCB process. The PCB material was Rogers 4350B with a dielectric constant of around 3.66 and a loss tangent of around 0.004 at 30 GHz. Though the dielectric loss tangent of Rogers 4350B was much larger than the Ferro A6M LTCC, it had a much lower prototype fabrication cost. Since the Rotman lens and WPD would occupy a considerable board area, the PCB process was selected for the fabrication of the beamforming network from a cost perspective.

The photographs of the LTCC array board and beamforming network PCB board are illustrated in Fig. 18. Each antenna element in the array could be accessed and characterized independently by directly connecting the feeding coaxial cable to the LTCC array board. Other than the capability of single-element measurement, the array performance could also be characterized by assembling the LTCC array board and beamforming network PCB through the connector jacks. In addition, the array beam scanning performance could be characterized by feeding different input ports of the Rotman lens on the beamforming PCB. As demonstrated in Fig. 19, the S-parameters and radiation patterns of the antenna element and the entire array were measured through the VNA and the μ-lab mmWave anechoic chamber, respectively.

A. MEASUREMENT RESULTS AND ANALYSIS OF SINGLE ELEMENT

Fig. 20 illustrates the comparisons between measured and simulated S-parameters of a single antenna element. In

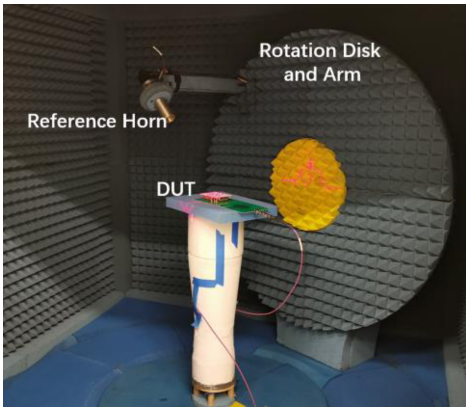

FIGURE 19. Phased array antenna measurement in μ-lab mmWave anechoic chamber.

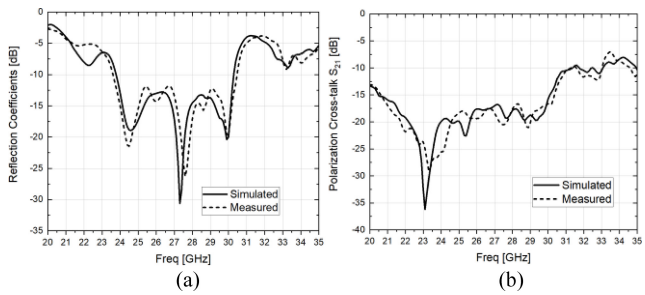

FIGURE 20. Simulation vs. measurement results of antenna element: (a) reflection coefficient, (b) polarizations crosstalk level.

both simulation and measurement, only the central antenna element was excited with the presence of all other surrounding zero-excitation array elements. Good agreements were achieved between the simulated and measured results. As demonstrated in Fig. 20(a), the antenna element achieved decent impedance matching in the frequency range of 23.6 to 30.4 GHz. Furthermore, the crosstalk level between two polarization ports of one antenna element was below –16 dB over the desired band from 24 to 30 GHz, as depicted in Fig. 20(b), indicating good isolation between the two orthogonal polarizations. Though good agreement has been achieved between measurements and simulations, there are still some obvious discrepancies, including the slight frequency shift (around 0.5 – 1 GHz) and some undesired ripples in the measured results. This is because the RF connector jack is not included in the simulation model and its multistage connection (RF feeding cable - RF adaptor - RF connector jacks - grounded GSG pads on LTCC board) can potentially introduce additional reflections and thus affect the measured S-parameters.

Fig. 21 illustrates the comparisons between measured and simulated radiation patterns of the single antenna element in both the E- and H-planes. The measured results matched well with the simulated results, especially in the boresight. However, as moving to the higher frequency range, there were more ripples in the radiation patterns, especially in E-plane. This was because the presence of surrounding elements, which had zero-excitations and were

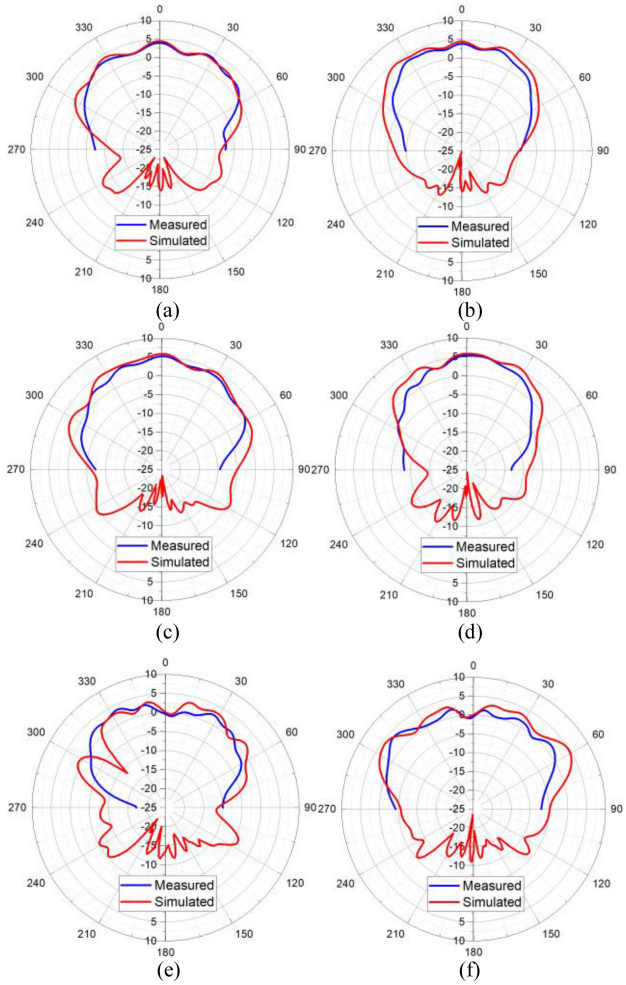

FIGURE 21. Simulated vs. measured results of antenna element radiation patterns. E-plane: (a) 24 GHz, (c) 27 GHz, and (e) 30 GHz. H-plane: (b) 24 GHz, (d) 27 GHz, and (f) 30 GHz.

not terminated with 50-ohm loads, behaved as multiple parasitic patches for the element under test. The mutual couplings induced undesired currents on the other elements that consequently deteriorated the radiation patterns of the element under test. In addition, because the adjacent element spacing became electrically larger and larger when moving to the higher frequency, the induced currents on the surrounding patches caused more obvious distortions in the radiation patterns, especially the E-plane radiation patterns. This type of distortion naturally appears when only one, rather than all elements, is excited. However, this influence reduces as more elements in the array are excited. Therefore, as long as the measured radiation patterns match the simulated results, the overall array performance will be good and matched to the array simulations, as verified in the following subsection.

B. MEASUREMENT RESULTS AND ANALYSIS OF ENTIRE ARRAY

This subsection compares the overall array performance between the simulated and measured results. Fig. 22 demonstrates the measured radiation patterns when scanning the

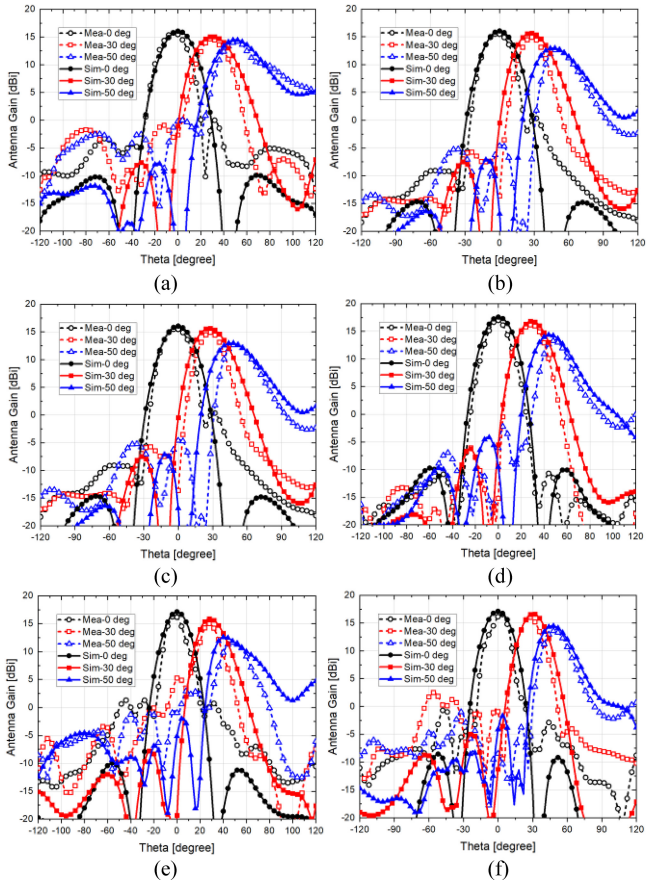

FIGURE 22. Phased array radiation patterns (beam scanning performance), measured versus simulated results: (a) E-plane at 24 GHz, (b) H-plane degrees at 24 GHz, (c) E-plane at 27 GHz, (d) H-plane at 27 GHz, (e) E-plane at 30 GHz, and (f) H-plane at 30 GHz.

main beam at different angles at 24, 27, and 30 GHz. The beam scanning performance was achieved by feeding from different beam ports on the Rotman lens. The fabricated phased array realized a maximum beam scanning capability of up to +/– 50 degrees in the two orthogonal planes over the desired frequency range of 24–30 GHz, which is a decent wide beam scanning range as particularly it is realized in the entire bandwidth with other performance aspects well maintained. The gain drop was around 3–3.3 dB when the main beam was scanning at +/–50 degrees. In the measurement, the maximum realized gain of 17.5 dB was achieved at 27 GHz. The simulated and measured results matched well, as demonstrated in Fig. 22. However, there was one apparent discrepancy: the measured maximum gain values were about 0.5–0.8 dB lower than the simulation results. This is because the connection jacks illustrated in Fig. 18 were not modeled in the simulation software to reduce the modeling complexity and simulation time. One connector jack had an insertion loss of around 0.6 dB in the operation frequency band.

In addition to the gain drop, another discrepancy between simulation and measurement is the narrow half-power beamwidth (HPBW) for all the measured beams. The reason for this discrepancy is an error in the fabrication. The LTCC board for this design has a relatively large size of 73.4 mm × 62.8 mm. Typically, during the LTCC fabrication process, the LTCC board experiences shrinkage in all directions. The different locations of the large LTCC board experience different shrinkage tensions. Consequently, our LTCC prototype has a slight concave bending on the top surface which leads to the array beams with narrower HPBM in the measurement.

VI. FIGURE OF MERIT

Considerable research efforts have been invested into designing mmWave 5G phased array design for base stations and small cells [7], [22], [38]. There are also many research studies on this topic in the literature. However, it is challenging to evaluate different designs' performance, since there are multiple design trade-offs, including operation bandwidths, numbers of elements, beam scanning ranges, realized antenna gains, polarization properties, and dimensions. There is not yet a benchmark or FoM for assessing the performance of a mmWave 5G phased array objectively. Thus, in this study, a novel FoM as a comprehensive metric to evaluate and contrast various mmWave 5G phased array architectures was proposed for the first time, considering all previously discussed factors.

There are two commonly used parameters to indicate the antenna system's transmission performance. The first one is aperture efficiency (ε_{ap}):

$$\varepsilon_{ap} = \frac{A_e}{A_p} = \frac{D_0}{D_{max}} \tag{4}$$

where A_e and A_p are the antenna's effective area and its physical area. D_0 and D_{max} are the antenna's directivity and the maximum directivity, respectively. The aperture efficiency measures how close the antenna comes to using all the RF power intersecting its physical aperture and can also indicate the sidelobe level and the grating lobe level in the array antenna.

The other parameter is radiation efficiency (e_r), which can reflect the conductor loss and dielectric loss of the antenna array:

$$e_r = \frac{G_0}{D_0} = \frac{G_0}{4\pi \frac{A_e}{\lambda^2}} = \frac{G_0 \lambda^2}{4\pi A_p \varepsilon_{ap}} \tag{5}$$

$$\eta_{ANT} = e_r \varepsilon_{ap} = \frac{G_0 \lambda^2}{4\pi A_p} = \frac{G_0 \lambda^2}{4\pi (Nd)^2} \tag{6}$$

where G_0 is the antenna gain, $N \times N$ is the number of antenna elements, and d is the element spacing. Therefore, the combination of these two parameters signifies how efficiently the antenna array handles the RF power transition between its terminal and open space. This combination is shaped by factors like the distance between elements, the total number of elements, and the array gain. In addition, the beam scanning range, bandwidth, array dimension, and the number of polarizations should be included in the

TABLE 3. FoM comparisons of the state-of-the-art 5G phased array designs.

Ref	Antenna Technology	FoM
[7]	Sequential rotation-fed dual-polarized patch	0.028
[8]	Probe-fed patch antenna	0.037
[9]	Parasitically gap-coupled patch	0.042
[10]	PCB-integrated stacked-patch antenna	0.051
[11]	Tightly coupled dipole array	0.083
[12, 13]	Slotted waveguide array	0.083
[14]	Air-cavity-backed patch antenna on lid substrate	0.114
[15]	Cavity-backed patch antenna	0.186
[16]	Dielectric resonator antenna arrays	0.198
[17]	Surface-mounted Vivaldi array	0.222
[18]	Coaxial-fed stacked patch antenna	0.259
[19]	Single-polarized surface-mounted Vivaldi array	0.265
[20]	Coaxial-fed stacked patch antenna	0.434
This work	Stacked patch with notched corners, EBG, and element rotation	0.451

FoM. The derivation of the proposed *FoM* appears in the following equation:

$$FoM = e_r\varepsilon_{ap} \times \frac{\Omega_{scan}}{\Omega_{Half-sphere}} \times \frac{\Delta f}{f_0} \times \frac{N^2\lambda^3}{\text{Volume}} \times Pol = \frac{G_0\lambda^5\Delta f \cdot Pol}{4\pi f_0 d^2 \cdot Volume} \cdot \frac{\Omega_{scan}}{\Omega_{Half-sphere}} \quad (7)$$

where Ω_{scan} and $\Omega_{Half-sphere}$ represent the calculated solid angles of an array's beam scanning range and the half-spherical space, respectively. The ratio of the two solid angles expresses the fraction of the half-spherical area that can be scanned by the phased array's main beam. In this equation, the operation bandwidth is also included as $\Delta f/f_0$. To evaluate the compactness of the array, this research introduced a density metric for the array. This metric is calculated as the inverse relationship between the total volume of the array and the same element numbers of half wavelength cubed as in (7). In the end, the number of polarizations (Pol) is also considered in the FoM to characterize the polarization performance.

Based on the obtained FoM, the comparison between this work and other state-of-art mmWave 5G phased arrays was concluded, as demonstrated in Table 3. The papers presented in Table 1 were also compared with the FoM. Notably, the proposed design reaches the highest value in the FoM compared with other state-of-the-art designs.

VII. CONCLUSION

The phased arrays for mmWave 5G communication require multiple simultaneous features, such as wide bandwidth for all performance parameters, high gain, dual-polarization, and wide beam scanning capability. However, this is a challenging task. This paper presents several design methodologies to concurrently optimize the phased array from all angles for the whole bandwidth. A 5×5 rectangular phased array was developed and constructed in a multilayered LTCC substrate. A dual linear polarized stacked patch antenna with notched corners was designed as the phased array's element for wideband performance. Additionally, to provide a wide beam-scanning range while reducing mutual couplings between the adjacent array elements, the orientations of all antenna elements were tuned, and EBG structures were designed and placed between antenna elements. Moreover, a wideband beamforming network, incorporating a Rotman lens coupled with five 5-way WPDs, has been developed and tested to validate the wide bandwidth and wide beam steering potential of the proposed antenna array. The proposed array design effectively encompasses the three most promising mmWave 5G frequency bands with the features of dual-polarization, high gain, and wide beam scanning potential. This positions it as a suitable option for the current rollout of mmWave 5G technology. A novel FoM was also proposed for an objective comparison and evaluation of various mmWave 5G phased array designs.

REFERENCES

[1] D. Witkowski, *Bridging the Gap-21st Century Wireless Telecommunications Handbook*, 2nd Ed. Scotts Valley, CA, USA: CreateSpace Independ. Publ. Platform, 2019.

[2] "IMT Vision–Framework and overall objectives of the future development of IMT for 2020 and beyond," ITU, Geneva, Switzerland, ITU-R Recommendation M.2083-0, 2015.

[3] C. E. Shannon, "Communication in the presence of noise," *Proc. IRE*, vol. 37, no. 1, pp. 10–21, Jan. 1949.

[4] "User equipment (UE) radio transmission and reception; Part 2: Range 2 standalone," 3GPP, Sophia Antipolis, France, 3GPP Rep. NR 38.101–2, 2020.

[5] A. N. Uwaechia and N. M. Mahyuddin, "A comprehensive survey on millimeter wave communications for fifth-generation wireless networks: Feasibility and challenges," *IEEE Access*, vol. 8, pp. 62367–62414, 2020.

[6] T. S. Rappaport, Y. Xing, G. R. MacCartney, A. F. Molisch, E. Mellios, and J. Zhang, "Overview of millimeter wave communications for fifth-generation (5G) wireless networks—With a focus on propagation models," *IEEE Trans. Antennas Propag.*, vol. 65, no. 12, pp. 6213–6230, Dec. 2017.

[7] X. Luo et al., "A scalable Ka-band 1024-element transmit dual-circularly-polarized planar phased array for SATCOM application," *IEEE Access*, vol. 8, pp. 156084–156095, 2020.

[8] K. Kibaroglu, M. Sayginer, and G. M. Rebeiz, "A low-cost scalable 32-element 28-GHz phased array transceiver for 5G communication links based on a 2 × 2 beamformer flip-chip unit cell," *IEEE J. Solid-State Circuits*, vol. 53, no. 5, pp. 1260–1274, May 2018.

[9] R. Valkonen, "Compact 28-GHz phased array antenna for 5G access," in *Proc. IEEE/MTT-S Int. Microw. Symp.*, 2018, pp. 1334–1337.

[10] K. Kibaroglu, M. Sayginer, T. Phelps, and G. M. Rebeiz, "A 64-element 28-GHz phased-array transceiver with 52-dBm EIRP and 8–12-Gb/s 5G link at 300 meters without any calibration," *IEEE Trans. Microw. Theory Techn.*, vol. 66, no. 12, pp. 5796–5811, Dec. 2018.

[11] S. Hussain, S. W. Qu, W. L. Zhou, P. Zhang, and S. Yang, "Design and fabrication of wideband dual-polarized dipole array for 5G wireless systems," *IEEE Access*, vol. 8, pp. 65155–65163, 2020.

[12] C. Bencivenni, M. Gustafsson, A. Haddadi, A. U. Zaman, and T. Emanuelsson, "5G mmWave beam steering antenna development and testing," in *Proc. 13th Eur. Conf. Antennas Propag. (EuCAP)*, 2019, pp. 1–4.

[13] C. Bencivenni, A. U. Zaman, A. Haddadi, and T. Emanuelsson, "Towards integrated active antennas for 5G mm-wave applications at gapwaves," in *Proc. IEEE Int. Symp. Antennas Propag. USNC/URSI Nat. Radio Sci. Meeting*, 2018, pp. 415–416.

[14] X. Gu et al., "Development, implementation, and characterization of a 64-element dual-polarized phased-array antenna module for 28-GHz high-speed data communications," *IEEE Trans. Microw. Theory Techn.*, vol. 67, no. 7, pp. 2975–2984, Jul. 2019.

[15] H. T. Kim et al., "A 28-GHz CMOS direct conversion transceiver with packaged 2×4 antenna array for 5G cellular system," *IEEE J. Solid-State Circuits*, vol. 53, no. 5, pp. 1245–1259, May 2018.

[16] D. Caratelli, A. Al-Rawi, J. Song, and D. Favreau, "Dielectric resonator antenna arrays for 5G wireless communications," (in English), *Microw. J.*, vol. 63, no. 2, pp. 36–46, Feb. 2020.

[17] H. Kähkönen, J. Ala-Laurinaho, and V. Viikari, "Surface-mounted ka-band vivaldi antenna array," *IEEE Open J. Antennas Propag.*, vol. 2, pp. 126–137, 2021.

[18] Y. Yin, B. Ustundag, K. Kibaroglu, M. Sayginer, and G. M. Rebeiz, "Wideband 23.5–29.5-GHz phased arrays for multistandard 5G applications and carrier aggregation," *IEEE Trans. Microw. Theory Techn.*, vol. 69, no. 1, pp. 235–247, Jan. 2021.

[19] M. A. Elmansouri, G. R. Friedrichs, L. B. Boskovic, and D. S. Filipovic, "An X-band through ka-band thinned all-metal vivaldi phased array," *IEEE Trans. Antennas Propag.*, vol. 69, no. 11, pp. 7613–7623, Nov. 2021.

[20] K. K. Wei Low, S. Zihir, T. Kanar, and G. M. Rebeiz, "A 27–31-GHz 1024- element Ka-band SATCOM phased-array transmitter with 49.5-dBW peak EIRP, 1-dB AR, and ±70° beam scanning," *IEEE Trans. Microw. Theory Techn.*, vol. 70, no. 3, pp. 1757–1768, Mar. 2022.

[21] A. Shamim and H. Zhang, "Antenna-in-package designs in multilayered low-temperature co-fired ceramic platforms," in *Antenna-in-Package Technology and Applications*. Hoboken, NJ, USA: Wiley, 2020, pp. 147–178, doi: 10.1002/9781119556671.ch6.

[22] "Low temperature co-fired ceramic systems A6M/A6M-E high frequency LTCC tape system," Tech. Data Sheet, Ferro Corp., Mayfield Heights, OH, USA, Nov. 2015.

[23] R. Mailloux, *Phased Array Antenna Handbook*, 3rd ed. Morristown, NJ, USA: Artech, 2017.

[24] L. H. Kong, J. H. Zhang, V. Volski, S. Yan, and G. A. E. Vandenbosch, "EBG-based dielectric image guide For 5G applications," in *Proc. Int. Symp. Antennas Propag. (ISAP)*, 2019, pp. 1–3.

[25] O. Antonio, A. Bruce, P. Francesco de, and C. Samuel, "Planar EBGs: Fundamentals and design," in *PElectromagnetic Bandgap (EBG) Structures: Common Mode Filters for High Speed Digital Systems*. Hoboken, NJ, USA: Wiley, 2017, pp. 21–60.

[26] O. Ayop and M. K. A. Rahim, "Analysis of mushroom-like electromagnetic band gap structure using suspended transmission line technique," in *Proc. IEEE Int. RF & Microw. Conf.*, 2011, pp. 258–261.

[27] S. Trinh-Van, J. M. Lee, Y. Yang, K. Y. Lee, and K. C. Hwang, "A sidelobe-reduced, four-beam array antenna fed by a modified 4 × 4 butler matrix for 5G applications," *IEEE Trans. Antennas Propag.*, vol. 67, no. 7, pp. 4528–4536, Jul. 2019.

[28] K. Klionovski, M. S. Sharawi, and A. Shamim, "A dual-polarization-switched beam patch antenna array for millimeter-wave applications," *IEEE Trans. Antennas Propag.*, vol. 67, no. 5, pp. 3510–3515, May 2019.

[29] J. Li, C. He, H. Fan, and R. Jin, "Gain-equalized multibeam antenna fed by a compact dual-layer rotman lens at ka-band," *IEEE Trans. Antennas Propag.*, vol. 70, no. 3, pp. 2307–2311, Mar. 2022.

[30] Y. Yu, H. Luyen, and N. Behdad, "A wideband millimeter-wave rotman lens multibeam array using substrate integrated coaxial line (SICL) technology," *IEEE Trans. Antennas Propag.*, vol. 69, no. 11, pp. 7532–7542, Nov. 2021.

[31] J. Park, D. Baek, and J. G. Kim, "A 28 GHz 8-channel fully differential beamforming IC in 65nm CMOS process," in *Proc. 49th Eur. Microw. Conf. (EuMC)*, 2019, pp. 476–479.

[32] M. S. Ali, M. A. B. Abbasi, and N. Shoaib, "On the phase-aligned transmission lines of a mmWave 5G rotman lens based beamformer," in *Proc. 1st Int. Conf. Microw. Antennas Circuits (ICMAC)*, 2021, pp. 1–3.

[33] A. Eid, J. Hester, and M. M. Tentzeris, "A scalable high-gain and large-beamwidth mm-Wave harvesting approach for 5G-powered IoT," in *Proc. IEEE MTT-S Int. Microw. Symp. (IMS)*, 2019, pp. 1309–1312.

[34] T. Vo Dai and O. Kilic, "Compact Rotman lens structure configurations to support millimeter wave devices," *Progr. Electromagn. Res. B*, vol. 71, pp. 91–106, Jan. 2016.

[35] M. Salman, Y. Jang, J. Lim, D. Ahn, and S.-M. Han, "Novel Wilkinson power divider with an isolation resistor on a defected ground structure with improved isolation," *Appl. Sci.*, vol. 11, no. 9, p. 4148, 2021.

[36] P. V. Naidu, M. S. Charan, A. Kumar, D. Sharma, P. Sharma, and K. S. Harish, "Design of 5 way wide band Wilkinson power divider for 6 to 18 GHz applications," in *Proc. Progr. Electromagn. Res. Symp. (PIERS-Toyama)*, 2018, pp. 838–842.

[37] L. I. Parad and R. L. Moynihan, "Split-tee power divider," *IEEE Trans. Microw. Theory Techn.*, vol. 13, no. 1, pp. 91–95, Jan. 1965.

[38] H. Zhang and A. Shamim, "Phased array antenna-in-package design for true-wideband mmWave 5G communication," in *Proc. IEEE Int. Symp. Antennas Propag. USNC-URSI Radio Sci. Meeting (USNC-URSI)*, Portland, OR, USA, 2023, pp. 1557–1558.

HAORAN ZHANG (Student Member, IEEE) received the bachelor's degree in electrical engineering from the University of Electronic Science and Technology of China, Chengdu, China, in 2017, and the master's degree in electrical engineering from King Abdullah University Science and Technology, Saudi Arabia, in 2019, where he is currently pursuing the Ph.D. degree with the IMPACT Lab, Electrical Engineering Program. His research interests include mm-wave on-chip antenna design, antenna array design for 5G applications, and electrically small antenna design.

ATIF SHAMIM (Senior Member, IEEE) received the M.S. and Ph.D. degrees in electrical engineering from Carleton University, Canada, in 2004 and 2009, respectively. He was an NSERC Alexander Graham Bell Graduate Scholar with Carleton University from 2007 till 2009 and an NSERC Postdoctoral Fellow with Royal Military College Canada and KAUST from 2009 to 2010. In August 2010, he joined the Electrical and Computer Engineering Program with KAUST, where he is currently an Associate Professor and a Principal Investigator with IMPACT Lab. He was an invited Researcher with VTT Micro-Modules Research Center, Oulu, Finland, in 2006. He is an author/coauthor of 300 international publications, an inventor on more than 40 patents and has given close to 100 invited talks at various international forums. His research interests are in innovative antenna designs and their integration strategies with circuits and sensors for flexible and wearable wireless sensing systems through a combination of CMOS and additive manufacturing technologies. He was given the Ottawa Centre of Research Innovation Researcher of the Year Award in 2008 in Canada. His work on Wireless Dosimeter won the ITAC SMC Award at Canadian Microelectronics Corporation TEXPO in 2007. He also won numerous business-related awards, including 1st prize in Canada's National Business Plan Competition and was awarded OCRI Entrepreneur of the Year Award in 2010. His research work has won Best Paper Awards in IEEE ICMAC 2021, IEEE IMS 2016, IEEE MECAP 2016, IEEE EuWiT 2008, first prize in IEEE IMS 2019 3MT competition and IEEE AP-S Design Competition 2022, finalist/honorable mention prizes in IEEE AP-S Design Competition 2020, IEEE IMS 2017 (3MT competition), IEEE IMS 2014, IEEE APS 2005, and R. W. P. King prize for journal papers in IEEE TAP 2017 and 2020. He has won the King's Prize for the best innovation of the year in 2018 for his work on sensors for the oil industry. He founded the first IEEE AP/MTT chapter in Saudi Arabia in 2013 and served on the editorial board of IEEE TRANSACTIONS ON ANTENNAS AND PROPAGATION from 2013 to 2019, and as a Guest Editor for IEEE AWPL Special issue in 2019, and is currently serving as an Associate Editor for IEEE JOURNAL OF ELECTROMAGNETICS, RF AND MICROWAVES IN MEDICINE AND BIOLOGY. He serves on numerous IEEE committees, such as IEEE Technical Committees on Antenna Measurements (AP-S), Microwave Controls (MTT-S 13), and Additive Manufacturing (CRFID). He has been selected as a Distinguished Lecturer for IEEE AP-S from 2022 to 2024.